

Effect of Synthesis Conditions on the First Charge and Reversible Capacities of Lithium-Rich Layered Oxide Cathodes

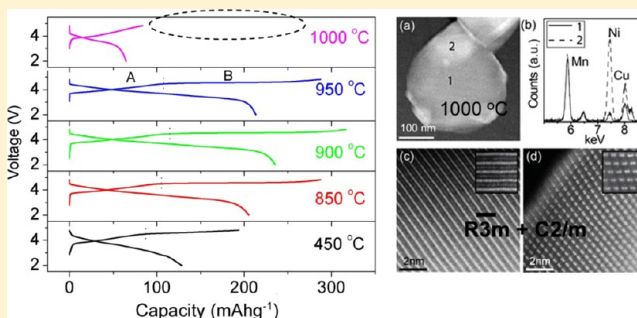
Chih-Chieh Wang, Karalee A. Jarvis, Paulo J. Ferreira, and Arumugam Manthiram*

Materials Science and Engineering Program, University of Texas at Austin, Austin, Texas 78712, United States

S Supporting Information

ABSTRACT: The influence of synthesis temperature and time on the length (capacity) of the plateau region during first charge in the high-capacity lithium-rich layered oxide $\text{Li}_{1.2}\text{Mn}_{0.6}\text{Ni}_{0.2}\text{O}_2$ and on the reversible capacity during subsequent charge–discharge cycles has been systematically investigated. The samples were synthesized by firing a sol–gel precursor obtained at 450 °C at various temperatures (850–1000 °C) for 24 h and at the optimum temperature of 900 °C for 6–72 h. The maximum length of the plateau region during the first charge and, consequently the maximum reversible capacity were achieved with the sample fired at 900 °C for 24 h. In contrast, the sample fired at 1000 °C for 24 h does not show any plateau region. In-depth characterization by X-ray diffraction, aberration-corrected transmission electron microscopy, scanning electron microscopy, inductively coupled plasma analysis, and electrochemical charge–discharge measurements reveals that the actual lithium content in the synthesized samples, compositional inhomogeneities, and the presence of a single C2/m phase vs a $\text{C2/m} + \text{R}\bar{3}\text{m}$ two-phase mixture play a critical role in the length of the plateau region, while particle size and surface area play a minor role. The study demonstrates the benefits of the formation of a single-phase C2/m solid solution with a lithium content of at least 1.16 in order to maximize the discharge capacity.

KEYWORDS: lithium-ion batteries, layered oxide cathodes, synthesis, crystal chemistry, electron microscopy



■ INTRODUCTION

Lithium-ion batteries are being widely used as energy storage devices in portable devices such as cell phones and laptop computers due to their high energy density. However, only 50% (140 mAh g^{−1}) of the theoretical capacity of the conventional layered LiCoO_2 cathode could be used in practical cells due to structural and chemical instabilities at deep charge.^{1,2} In this regard, solid solutions between layered LiMO_2 ($\text{M} = \text{Mn}, \text{Co}, \text{and Ni}$) and layered $\text{Li}[\text{Li}_{1/3}\text{Mn}_{2/3}]\text{O}_2$ (commonly designated as Li_2MnO_3) have become appealing in recent years as they exhibit much higher capacities ($\sim 250 \text{ mAh g}^{-1}$)^{3–10} compared to the commercially available cathodes, such as LiCoO_2 or $\text{LiNi}_{1-y-x}\text{Mn}_y\text{Co}_x\text{O}_2$.^{11,12} For example, $\text{Li}[\text{Li}_{1/3-2x/3}\text{Mn}_{2/3-x/3}\text{Ni}_x]\text{O}_2$ ($0 \leq x \leq 0.5$), a solid solution between $\text{Li}[\text{Li}_{1/3}\text{Mn}_{2/3}]\text{O}_2$ and $\text{Li}[\text{Mn}_{0.5}\text{Ni}_{0.5}]\text{O}_2$, exhibits capacities greater than 250 mAh g^{−1} on charging to 4.8 V.^{4–9} These solid solution cathodes with more than one lithium per formula unit are commonly referred to as lithium-rich layered oxides.

The remarkably high capacity achieved with this class of solid solution cathodes is due to an irreversible loss of oxygen from the layered lattice during first charge^{13,14} and/or oxidation of the transition-metal ions beyond 4+.¹⁵ Such redox processes during first charge result in a lowering of the oxidation state of the transition metal ions at the end of first discharge, which leads to a higher reversible capacity during subsequent cycling

involving the redox reactions of mainly the transition-metal ions. Since the reversible capacity depends on the length (capacity) of the plateau region during first charge, it is critical to have a clear understanding of the factors that control the length of the plateau region in this class of materials and use the understanding to maximize their electrochemical performance.

The length of the plateau region has been found, for instance, to be sensitively influenced by the substitution of other metal ions. For example, the length of the plateau region is suppressed by the substitution of Ti^{4+} for Mn^{4+} but increased by the substitution of Co^{3+} for equal amounts of Mn^{4+} and Ni^{2+} in $\text{Li}[\text{Li}_{0.2}\text{Mn}_{0.6}\text{Ni}_{0.2}]\text{O}_2$ due to the changes in the metal–oxygen covalence.^{16–18} Also, when oxygen is substituted by fluorine, the length of the plateau region is decreased due to the reduction in covalence (or increase in bond ionicity).¹⁹ However, to the best of our knowledge, the influence of synthesis conditions, such as firing temperature and time, on the length of the plateau region and reversible capacity has not been explored. We present here a systematic investigation of the influence of firing temperature (850–1000 °C) and firing time (6–72 h at 900 °C) on the oxygen loss behavior and capacity of the lithium-rich layered oxide composition

Received: July 3, 2013

Revised: July 4, 2013

Published: July 5, 2013



$\text{Li}_{1.2}\text{Mn}_{0.6}\text{Ni}_{0.2}\text{O}_2$. The samples are characterized by X-ray diffraction (XRD), scanning electron microscopy (SEM), aberration-corrected transmission electron microscopy (TEM), wet-chemical analysis, and electrochemical measurements to establish a correlation among phase composition, structure, and electrochemical properties.

EXPERIMENTAL SECTION

Synthesis. $\text{Li}_{1.2}\text{Mn}_{0.6}\text{Ni}_{0.2}\text{O}_2$ was prepared by a sol–gel method. Required amounts of lithium acetate (Acros Organics, 99% pure), manganese acetate (Acros Organics, 99% pure), and nickel acetate (Acros Organics, 99% pure) were first dissolved in deionized water. Ethylenediaminetetraacetic acid (EDTA; Acros Organics, 99% pure) and citric acid (Acros Organics, 99% pure), acting as complexing agents, were added to NH_4OH (Acros Organics, 28–30% in water) to form a homogeneous aqueous solution with a pH of ~ 8 . The metal acetate solution was then added to the EDTA/citric acid solution. The mole ratio of EDTA: citric acid: metal ion was 1: 1.5: 1. The mixture was then heated on a hot plate at 90 °C for 12 h until a gel was formed, which was then fired at 450 °C for 6 h to remove the organic residues. This resulting powder will hereafter be referred to as the precursor sample. To understand the influence of synthesis temperature, the 450 °C precursor sample was then fired at various temperatures (850, 900, 950, and 1000 °C) for 24 h. To understand the effect of synthesis time, the 450 °C precursor sample was fired at 900 °C for 6, 12, 24, 48, and 72 h. Since firing at higher temperatures resulted in a volatilization of part of the lithium, additional samples were also synthesized by adding a known amount of excess lithium to the reaction mixture to realize a specific or constant lithium content in the final product as discussed in the later sections.

Chemical and Structural Characterization. The lithium contents in the synthesized samples were determined by inductively couple plasma (ICP) analysis. XRD data were collected with a Philips X'pert diffractometer and Cu $K\alpha$ radiation in the 2θ range of 10–80° at an interval of 0.02°. The morphology and particle size of the samples were investigated with a JEOL JSM-5610 SEM. Further phase and compositional analyses were carried out with a JEOL 2010F TEM or JEOL ARM200F aberration corrected TEM/STEM equipped with a CEOS GmbH hexapole corrector for the illuminating lenses and a high-angle annular dark-field (HAADF) detector. For the compositional analysis, 50 particles in each sample were analyzed by energy dispersive spectroscopy (EDS) with the JEOL 2010F TEM. Some samples were further analyzed by EDS with the JEOL ARM200F TEM/STEM. Due to the low atomic number, lithium could not be detected with EDS. Furthermore, the Mn L-edge overlapped with the O k-edge in EDS, which made quantification of oxygen challenging. Therefore, nickel content measurements were taken against only Mn. A few high-resolution scanning transmission electron microscopy (STEM) images were deconvoluted to reduce noise using the maximum entropy method implemented by Ishizuka.²⁰ It should be noted that only the samples that needed further investigation beyond XRD for structural and compositional information were analyzed with TEM.

Electrochemical Characterization. Electrochemical performances were evaluated with 2032-type coin cells at 10 mA g^{-1} between 2 and 4.8 V. The coin cells were fabricated with the layered oxide cathode, lithium metal anode, 1 M LiPF_6 in ethylene carbonate/diethyl carbonate (v/v 1:1) electrolyte, and Celgard polypropylene separator. To make the cathode, a slurry consisting of 80 wt % active material, 10 wt % super p carbon, and 10 wt % polyvinylidene fluoride (PVDF) binder with *N*-methyl-2-pyrrolidone (NMP) as the solvent was made and then casted onto an aluminum foil. The casted cathode was dried in an air oven at 80 °C for 3 h and then under vacuum at 120 °C for 12 h. After drying, cathode disks of 0.64 cm^2 area were punched out to assemble the coin cells. The electrodes consisted of a similar active material loading of 6.5 ± 0.5 mg.

RESULTS AND DISCUSSION

1. Crystal Chemistry and Microstructure. 1.1. Effect of Synthesis Temperature.

Figure 1 shows the XRD patterns of the

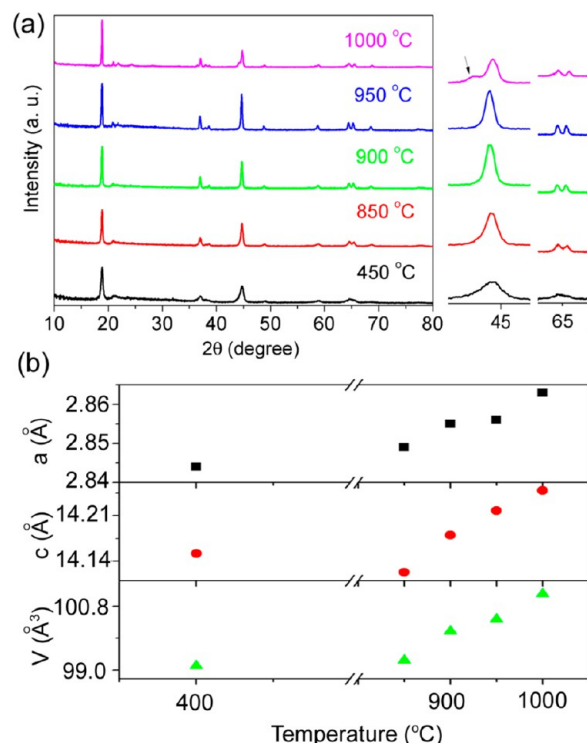


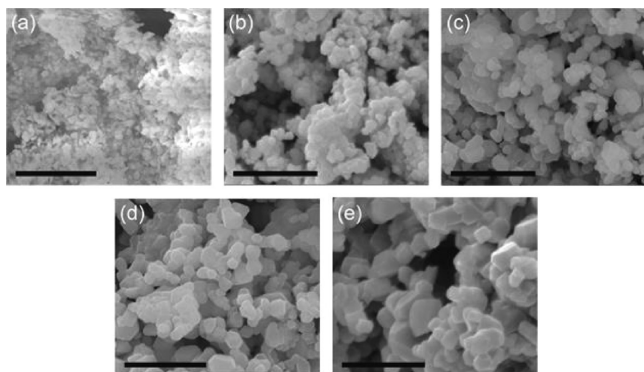
Figure 1. (a) XRD patterns of the $\text{Li}_{1.2}\text{Mn}_{0.6}\text{Ni}_{0.2}\text{O}_2$ sample fired at various temperatures for 24 h and (b) variation of lattice parameters with firing temperature.

the samples fired at 850, 900, 950, and 1000 °C for 24 h along with the precursor sample heated at 450 °C. The reflections of the 850–1000 °C samples are characteristic of the layered α - NaFeO_2 structure. With the exception of the 1000 °C sample, the reflections around 65° (Figure 1a) become sharper with increasing temperature, indicating a better-formed layered oxide.^{21–24} The reflections shifts to lower angle and the lattice parameters increase with increasing synthesis temperature as seen in Figure 1b due to the volatilization of lithium (Table 1) and the consequent reduction of smaller Mn^{4+} ions (0.53 Å) to larger Mn^{3+} ions (0.58 Å); as seen in Table 1, the experimental Mn and Ni contents are similar to the nominal values. The sample fired at 1000 °C shows an additional reflection at 44.2° , as indicated by an arrow in Figure 1a, compared to the other samples, which will be explained later. The superstructure reflections at 20 – 25° become more pronounced as the firing temperature increases to 1000 °C (Figure 1a), which could be related to an increasing degree of lithium–ion ordering in the transition metal layer ($\text{C}2/m$ phase), particle size, and amount of planar defects on the transition metal layer.^{25–27} Therefore, further electron microscopy characterization was carried out to determine the morphology, particle size, and degree of lithium–ion ordering ($\text{C}2/m$ phase) in the transition metal layers. The SEM images in Figure 2 show a polyhedral morphology for all the samples fired at 450, 850, 900, 950, and 1000 °C. The particle size increases from 100 nm to ~ 1 μm and the surface area decreases from 3.8 to 1.4 $\text{m}^2 \text{g}^{-1}$ (Table 1) with increasing synthesis temperature.

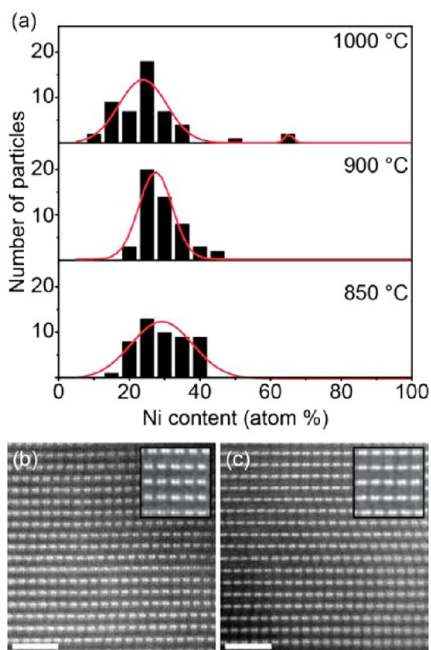
Table 1. Compositional and Electrochemical Data of $\text{Li}_{1.2}\text{Mn}_{0.6}\text{Ni}_{0.2}\text{O}_2$ Fired at Various Temperatures for 24 h

temp (°C)	exptl metal-ion content			surface area ($\text{m}^2 \text{g}^{-1}$)	theor. first charge capacity (mAh g^{-1})		exptl first charge capacity (mAh g^{-1})	
	Li	Mn	Ni		sloping region ^a	plateau region ^b	sloping region	plateau region
450	1.21	0.60	0.196		124	258	90	103
850	1.17	0.60	0.197	3.8	124	246	116	171
900	1.16	0.60	0.195	3.6	124	244	121	195
950	1.15	0.60	0.195	2.4	124	241	119	167
1000	1.09	0.60	0.194	1.4	124	225	84	-

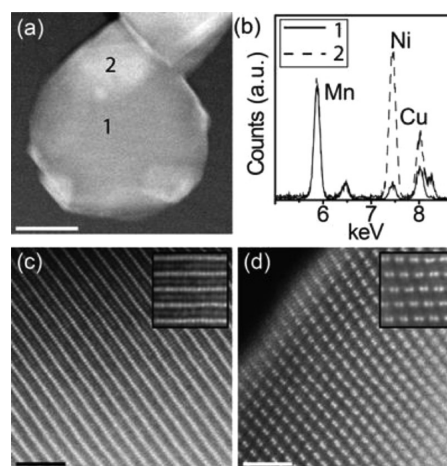
^aCalculated by assuming oxidation of Mn and Ni, respectively, to Mn^{4+} and Ni^{4+} with no oxygen loss or no oxidation of transition-metal ions beyond 4+ and a nominal formula of $\text{Li}_{1.2}\text{Mn}_{0.6}\text{Ni}_{0.2}\text{O}_2$. ^bCalculated by subtracting the theoretical capacity in the sloping region from the total theoretical capacity for extracting all the lithium from the lattice.

**Figure 2.** Secondary electron SEM images of $\text{Li}_{1.2}\text{Mn}_{0.6}\text{Ni}_{0.2}\text{O}_2$ after firing at (a) 450, (b) 850, (c) 900, (d) 950, and (e) 1000 °C for 24 h. The scale bars are 2 μm .

TEM analysis shows that both the 850 and 900 °C samples are composed of the $\text{C2}/m$ phase (Figure 3), which is consistent with our previous TEM analysis of the 900 °C

**Figure 3.** (a) Particle count as a function of nickel content measured with EDS for the $\text{Li}_{1.2}\text{Mn}_{0.6}\text{Ni}_{0.2}\text{O}_2$ sample fired at various temperatures for 24 h. STEM images of $\text{Li}_{1.2}\text{Mn}_{0.6}\text{Ni}_{0.2}\text{O}_2$ fired at (b) 850 and (c) 900 °C for 24 h. The scale bars are 2 nm. The insets show deconvoluted images at higher magnifications.¹⁸ The nickel content was measured against Mn only.

sample.²⁸ Clearly, the sample becomes more homogeneous on going from 850 to 900 °C, as indicated by the EDS analysis (Figure 3a). In contrast, the 1000 °C sample becomes very inhomogeneous from particle to particle. Also, large variations in HAADF-STEM contrast (Figure 4a) and composition

**Figure 4.** (a) STEM image of $\text{Li}_{1.2}\text{Mn}_{0.6}\text{Ni}_{0.2}\text{O}_2$ fired at 1000 °C for 24 h and (b) EDS spectra averaged over the dark areas (1) and the bright areas (2) normalized to the Mn peak. The scale bar is 100 nm. STEM image of $\text{Li}_{1.2}\text{Mn}_{0.6}\text{Ni}_{0.2}\text{O}_2$ fired at 1000 °C for 24 h, taken from an area (a) high in nickel and (d) high in lithium. The scale bars are 2 nm. The insets show deconvoluted images at higher magnifications.¹⁸ The Cu peak in (b) arises from the sample support grid.

(Figure 4b) are seen within a single particle. The contrast in HAADF-STEM imaging is directly related to the relative atomic number by a factor of $\sim Z^{1.7}$ (Z = atomic number).²⁹ Therefore, the brighter areas should be higher in transition metal content and lower in lithium content. EDS analysis shows that the atomic percentage of nickel relative to manganese increases significantly in the bright areas (Figure 4b). We, therefore, conclude that the brighter contrast of Figure 4a results from an increase in nickel and a decrease in lithium content. These changes in composition result in different phases (Figure 4c,d). In particular, regions with higher nickel content (bright contrast) show no lithium ordering in the transition metal layer, which results in an $\text{R}\bar{3}m$ phase with some interlayer mixing (Figure 4c), while the areas with more lithium (darker contrast) exhibit a $\text{C2}/m$ phase (Figure 4d). The $\text{R}\bar{3}m$ and $\text{C2}/m$ phases in the 1000 °C sample segregate into large domains (>50 nm). Due to the large size of each phase, an XRD peak at about 44.2° could be expected from the $\text{R}\bar{3}m$ phase of LiMO_2 and an XRD peak at about 44.8° could appear due to the $\text{C2}/m$ phase of Li_2MnO_3 . In fact, we see that the

pronounced peak around 45° in the XRD pattern has shifted from about 44.7° in the 950°C sample to 44.8° in the 1000°C sample and the asymmetric peak resides at about 44.2° (Figure 1c). It can, therefore, be concluded that the shoulder present on the 44.8° peak in the 1000°C sample results from areas of LiMO_2 ($R\bar{3}m$ phase), and the sharp peak at 44.8° results from areas of Li_2MnO_3 ($C2/m$ phase). Overall, the sample consists $R\bar{3}m$ and $C2/m$ phases due to large variations in composition. The large variations in composition and phase separation occur due to the loss of a significant amount of lithium at 1000°C (Table 1).

To further understand the role of lithium content, the 1000°C sample was synthesized by taking an excess amount of lithium in the reaction mixture and firing the mixture at 1000°C for 24 h. This 1000°C sample was found to have a lithium content of 1.16, as indicated by the ICP analysis. Although this sample is more homogeneous in composition from particle to particle (Figure 5a), it still shows the two phases ($R\bar{3}m$ and $C2/m$)

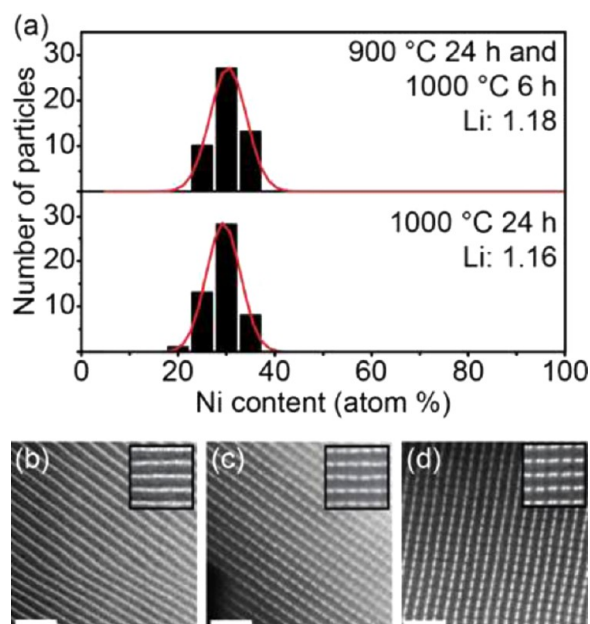


Figure 5. (a) Particle count as a function of nickel content measured with EDS for lithium-rich layered oxides with experimental lithium contents of 1.16 and 1.18 obtained by firing at 1000°C for 24 h and 900°C for 24 h followed by at 1000°C for 6 h, respectively. (b and c) STEM images of the above sample with a lithium content of 1.16 from two different areas of the same particle. (d) STEM image of the above sample with a lithium content of 1.18. The scale bars are 2 nm. The insets show deconvoluted images at higher magnifications.¹⁸ The nickel content was measured against Mn only.

m) within individual particles (Figure 5b,c), indicating local compositional variations. Thus, adjusting for lithium loss during heat treatment at 1000°C improves the homogeneity between particles but is still not sufficient to fully homogenize the individual particles. To ensure full homogeneity, another sample with an excess amount of lithium was first fired at 900°C for 24 h and then fired at 1000°C for 6 h. This sample with a lithium content of 1.18 shows good homogeneity from particle to particle (Figure 5a) and within individual particles (Figure 5d), and it was found to be composed of a single $C2/m$ phase. The results demonstrate that the synthesis of lithium-rich layered oxides at high temperatures, such as 1000°C , is

prone to lithium loss, compositional inhomogeneities, and phase segregation.

1.3. Effect of Synthesis Time. Figure 6a shows the XRD patterns of the samples fired at 900°C for 6, 12, 24, 48, and 72 h

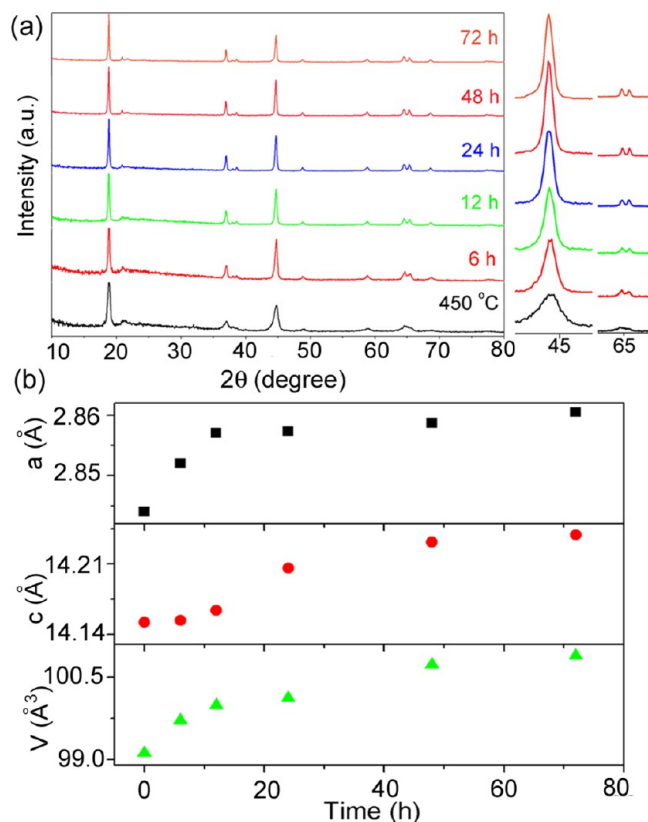


Figure 6. (a) XRD patterns of the $\text{Li}_{1.2}\text{Mn}_{0.6}\text{Ni}_{0.2}\text{O}_2$ sample fired at 900°C for various times and (b) variation of lattice parameters with firing time.

h along with the 450°C precursor sample. The reflections shift to lower angles and the lattice parameter increases with increasing firing time (Figure 6b) due to the loss of lithium from the lattice (Table 2) and the consequent reduction of smaller Mn^{4+} ions into larger Mn^{3+} ions. The reflections around 65° become sharper and separate into two distinct peaks as the heating time increases, indicating a better cation ordering between the lithium and transition-metal planes. Also, the superstructure reflections at $20\text{--}25^\circ$ become sharper with increasing synthesis time. The SEM images in Figure 7 reveal that all the samples have a polyhedral morphology, and the particle size increases from 100 to 500 nm with increasing firing time. The surface area decreases from $4.4\text{ m}^2\text{ g}^{-1}$ for the 6 h sample to $3.1 \pm 0.5\text{ m}^2\text{ g}^{-1}$ for the 12–72 h samples (Table 2).

Figure 8a shows that increasing the firing time slightly improves the homogeneity from particle to particle. For samples heated under 72 h, HAADF-STEM imaging shows that the samples are composed of the $C2/m$ phase (Figure 8b–d). The 72 h sample, however, is composed of both the $R\bar{3}m$ and $C2/m$ phases with cation mixing between the lithium and transition-metal layers (Figure 8e). This is due to the loss of lithium during the prolonged heat treatment (Table 2). Unlike in the 1000°C sample, the $R\bar{3}m$ and $C2/m$ phases are integrated at the nanometer scale in the 900°C sample fired for 72 h. Interestingly, there is only one peak around 44.7° in the

Table 2. Compositional and Electrochemical Data of $\text{Li}_{1.2}\text{Mn}_{0.6}\text{Ni}_{0.2}\text{O}_2$ Fired at 900 °C for Various Times

time (h)	exptl metal-ion content			surface area ($\text{m}^2 \text{g}^{-1}$)	theor. first charge capacity (mAh g^{-1})		exptl first charge capacity (mAh g^{-1})	
	Li	Mn	Ni		sloping region ^a	plateau region ^b	sloping region ^a	plateau region ^b
6	1.20	0.60	0.198	4.4	124	254	101	184
12	1.18	0.60	0.201	2.7	126	244	120	190
24	1.16	0.60	0.196	3.6	124	244	121	195
48	1.15	0.60	0.195	2.9	124	240	123	182
72	1.11	0.60	0.197	3.0	124	228	98	142

^aCalculated by assuming oxidation of Mn and Ni, respectively, to Mn^{4+} and Ni^{4+} with no oxygen loss or no oxidation of transition-metal ions beyond 4+ and a nominal formula of $\text{Li}_{1.2}\text{Mn}_{0.6}\text{Ni}_{0.2}\text{O}_2$. ^bCalculated by subtracting the theoretical capacity in the sloping region from the total theoretical capacity for extracting all the lithium from the lattice

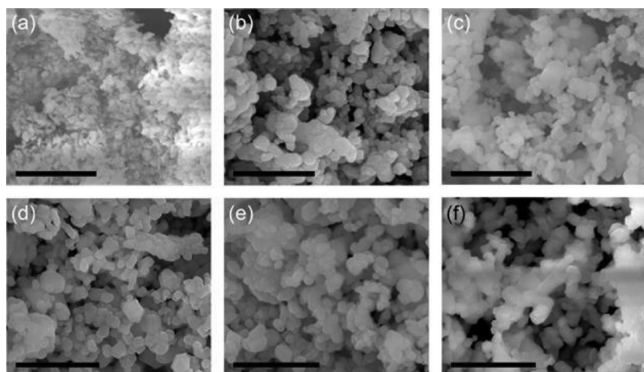


Figure 7. Secondary electron SEM images of $\text{Li}_{1.2}\text{Mn}_{0.6}\text{Ni}_{0.2}\text{O}_2$ after firing at (a) 400 °C for 24 h and at 900 °C for (b) 6, (c) 12, (d) 24, (e) 48, and (f) 72 h. The scale bars are 2 μm .

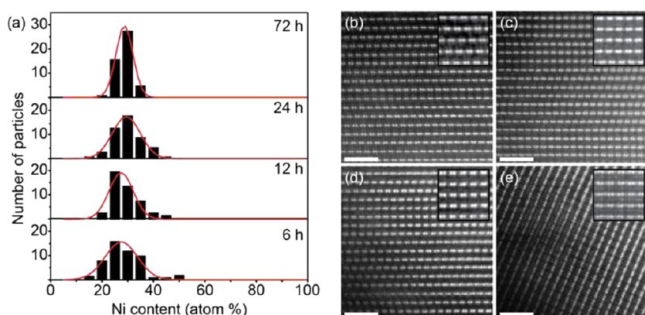


Figure 8. (a) Particle count as a function of nickel content measured with EDS for $\text{Li}_{1.2}\text{Mn}_{0.6}\text{Ni}_{0.2}\text{O}_2$ fired at 900 °C for various times. STEM images of $\text{Li}_{1.2}\text{Mn}_{0.6}\text{Ni}_{0.2}\text{O}_2$ fired at 900 °C for (b) 6, (c) 12, (d) 24, and (e) 72 h. The scale bars are 2 nm. The insets show deconvoluted images at higher magnifications.¹⁸ The nickel content was measured against Mn only.

XRD pattern of this sample (Figure 6a), in contrast to the XRD pattern of the 1000 °C sample, which results from the integration of the two phases at the nanometer scale.

It is important to note that the samples that contain primarily the $C2/m$ phase (850 °C sample and the 900 °C sample fired for 6–24 h) have broader and less intense XRD peaks compared to the samples containing both the $C2/m$ and $R\bar{3}m$ phases (1000 °C sample and the 900 °C sample heated for 72 h). This means that the increase in the intensities of the peaks at 20–25° of the samples heated at 1000 °C for 24 h and at 900 °C for 72 h does not result from an increase in the amount of the $C2/m$ phase. As mentioned above, particle size and planar defects can also affect the sharpness of these peaks. While the particle size of the 1000 °C sample is much larger than that of the 900 °C sample, the particle size of the 900 °C sample fired

for 72 h is not much larger than that of the sample fired for 24 h; nevertheless, both the samples show an increase in the sharpness of the XRD peaks in the 20–25° range. Thus, the effect of planar defects was examined in greater detail. Selected area electron diffraction (Figure 9) shows that as the firing

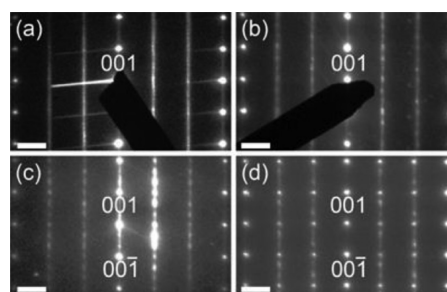


Figure 9. SAD patterns of $\text{Li}_{1.2}\text{Mn}_{0.6}\text{Ni}_{0.2}\text{O}_2$ fired at (a) 900 °C for 12 h, (b) 900 °C for 24 h, (c) 900 °C for 72 h, and (d) 1000 °C for 24 h. The scale bars are 2 nm^{-1} . Due to the presence of planar defects, only the $(001)_M$ reflections have been labeled.

temperature and time increase, the diffraction peaks related to the $C2/m$ phase become sharper and have fewer streaks, indicating less planar defects.^{27,30,31} We can, therefore, infer that the more pronounced $C2/m$ superlattice reflections in the 20–25° range are predominantly due to a decrease in the fraction of planar defects and not due to a decrease in lithium ordering in the transition metal layer.

2. Electrochemical Properties. 2.2. Effect of Synthesis Temperature. Figure 10a shows the first charge–discharge profiles of the samples fired at various temperatures for 24 h. The first charge capacity in the sloping region (A) increases with increasing firing temperature up to 900 °C and then decreases. The capacity increase in the sloping region is due to the well-formed layered oxides, as confirmed by the splitting of the peaks around 65° (Figure 1a). However, for synthesis temperatures higher than 900 °C, the capacity in the sloping region shows a slight decrease. This may be attributed to the cation disorder between the transition metal and lithium layers in some areas, caused by a lower lithium content arising from the volatilization of lithium during firing at higher temperatures. The plateau region also increases with increasing synthesis temperatures up to 900 °C. The observed plateau region is lower than the theoretical values shown in Table 1, implying that not all lithium ions were extracted from the lattice during the first charge. Interestingly, the plateau region completely disappeared for the 1000 °C sample. This can be understood by considering the changes in lithium content, phase relationships, particle size, and surface area. It appears that the $C2/m$ phase is essential to realize the plateau region in

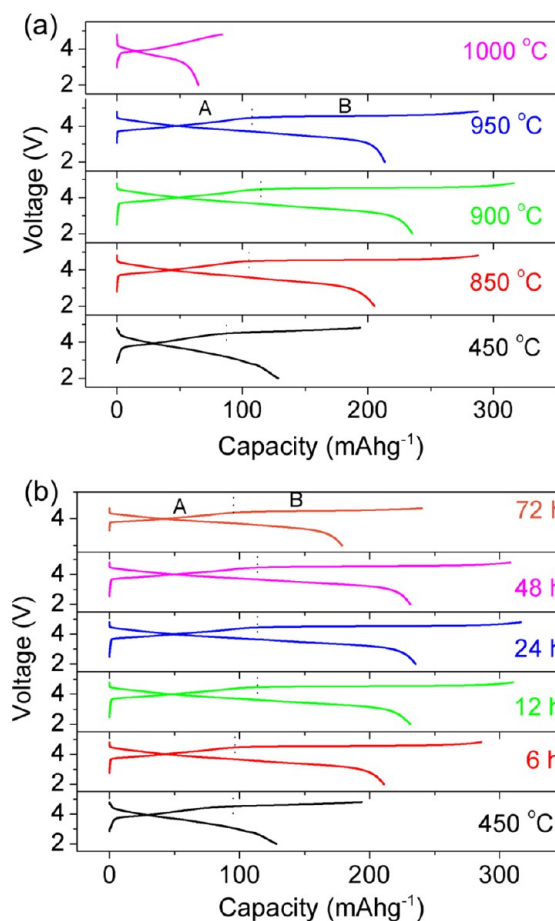


Figure 10. First charge–discharge profiles of $\text{Li}_{1.2}\text{Mn}_{0.6}\text{Ni}_{0.2}\text{O}_2$ (a) after firing at various temperatures for 24 h and (b) after firing at 900 °C for 6, 12, 24, 48, and 72 h when cycled from 2 to 4.8 V at 10 mA g^{-1} .

lithium-rich oxides. Both the segregation into the $R\bar{3}m$ and $C2/m$ phases in the 1000 °C sample along with the much larger particle size or smaller surface area, which could suppress the diffusion of oxygen vacancies and cations from the surface to the bulk, lead to a vanishing of the plateau region in the 1000 °C sample. Armstrong et al.¹³ have shown that the plateau region involves a significant diffusion of oxide ions and cations from the surface to the bulk accompanied by a condensation of the cation and oxide-ion vacancies.

In order to further understand the effect of lithium content on the capacity in the plateau region, samples with a higher lithium content were also synthesized at 1000 °C by taking an excess amount of lithium in the reaction mixture. The first charge–discharge profiles in Figure 11a show that the plateau region of the 1000 °C sample appears when the lithium content is increased. However, even though the lithium content is similar to that of the 900 °C sample, the capacity in the plateau region is still much lower for the 1000 °C sample. Jo et al.³² suggested that layered oxides with different particle sizes charged at low C rates do not significantly impact the charge capacity. Their results show that at C/10 rate, only a 10 mAh g^{-1} difference in the charge capacity is observed for particles with sizes increasing from 300 nm to 1 μm . In our case, the difference in particle size between the 900 and 1000 °C samples is ~ 400 nm and the C rate is relatively low (1/25 C). However, they exhibit a difference of 91 mAh g^{-1} in capacity. Therefore,

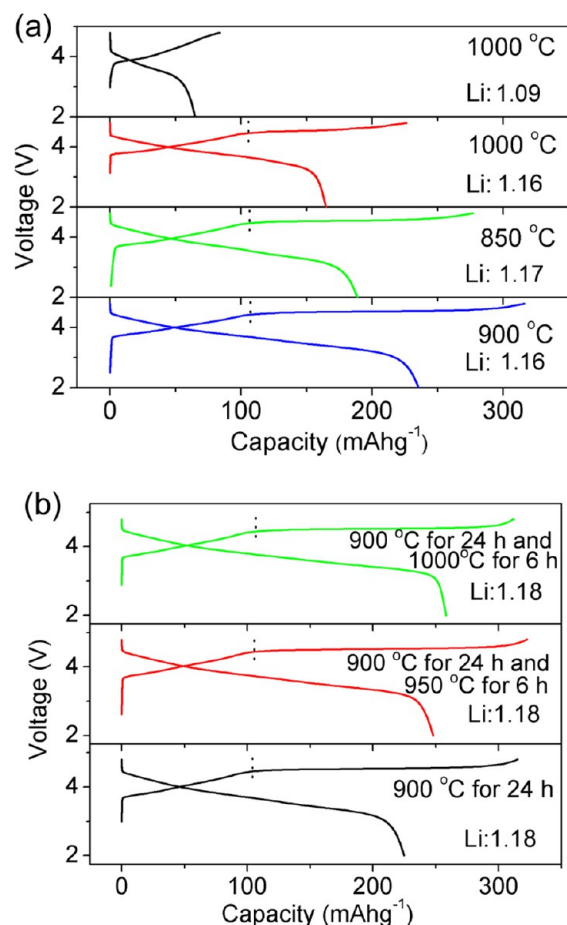


Figure 11. (a) First charge–discharge profiles of lithium-rich layered oxides with similar experimental lithium contents of ~ 1.16 in comparison to the 1000 °C sample with a Li content of 1.09 when cycled from 2 to 4.8 V at 10 mA g^{-1} . (b) First charge–discharge cycles of lithium-rich layered oxides with similar lithium contents of 1.18 after firing at 900 °C for 24 h, 900 °C for 24 h followed by at 950 °C for 6 h, and 900 °C for 24 h followed by at 1000 °C for 6 h when cycled from 2 to 4.8 V at 10 mA g^{-1} .

the large difference in capacity need not be directly related to the particle size effect. One possible explanation is the presence of both the $R\bar{3}m$ and $C2/m$ phases in the 1000 °C sample (Figure 4). When the sample is composed of pure $C2/m$ phase, as in the case of the sample fired at 900 °C for 24 h followed by at 1000 °C for 6 h (Figure 5d), the plateau region increases and is nearly identical to that of the 900 °C sample (Figure 11b). Yet, the particle size grows from 400 to 800 nm as shown in Figure S1. This implies that the types of phases present in the lithium-rich layered oxide plays a crucial role in determining the length of the plateau region. Furthermore, the discharge capacity of the sample fired at 900 °C for 24 h followed by at 1000 °C for 6 h is larger than that of the sample directly fired at 1000 °C for 24 h, even though both have the same lithium content (1.18). The increase in the discharge capacity can be attributed to the decrease in interlayer mixing between nickel and lithium ions after post heat treatment, as evident from the XRD data in Figure 12, i.e., the diffraction peaks at 65° become sharper with more splitting for the sample fired at 900 °C for 24 h followed by at 1000 °C for 6 h, compared to that for the sample fired at 900 °C for 24 h. Thus, the highest charge and discharge capacity is achieved when the sample is a

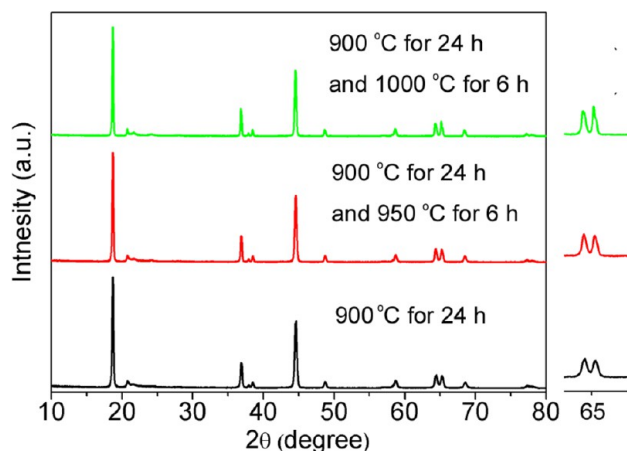


Figure 12. XRD patterns of lithium-rich layered oxides with similar lithium contents of ~ 1.18 after heating at 900 °C for 24 h, 900 °C for 24 h followed by at 950 °C for 6 h, and 900 °C for 24 h followed by at 1000 °C for 6 h.

homogeneous single $C2/m$ phase with little or low interlayer mixing between nickel and lithium ions.

2.3. Effect of Synthesis Time. The first charge–discharge capacity profiles of the samples fired at 900 °C for various times are shown in Figure 10b. The sloping region (A) increases with synthesis time up to 48 h, after which, it decreases with further increase in time. The decrease is due to an increase in the cation mixing as observed in Figure 8e. The plateau region in the first charge cycle increases as the firing time increases to 24 h. The increase in the plateau region may be due to an improved homogeneity and less interlayer mixing. The plateau region is slightly shorter for the 48 h sample, despite the presence of well-defined peaks in the 20° – 25° range. This may be due to the growth of the particles from 300 to 400 nm with decreased surface area³³ and a decrease in the lithium content. Interestingly, the capacity in the plateau region decreases by 50 mAh g^{-1} on going from a 48 h to a 72 h synthesis time even though the particle grows only slightly from 400 to 500 nm and the lithium content decreases only by 0.04. The decrease in the plateau region of the 72 h sample could be due to the decrease in the amount of $C2/m$ phase and the presence of the $R\bar{3}m$ phase (Figure 8e).

2.4. Effect of Heating Rate. Besides the firing temperature and time, the first charge–discharge capacities of the samples cooled with different cooling rates were also examined as shown in Figure S1. Clearly, the cooling rate does not have a pronounced effect on the oxygen loss behavior in lithium-rich layered oxides.

3. Cyclability, Columbic Efficiency, and Rate Capability. Figures 13 shows the cyclability and columbic efficiency of the samples fired at different temperatures and for different durations. Interestingly, the capacity of the samples fired at 950 and 1000 °C for 24 h and the sample fired at 900 °C for 72 h increase with increasing cycle number and become stable after a specific number of cycles. This could be due to the particle size effect^{34,35} since the larger particle size could limit lithium-ion diffusion, which may become alleviated with increasing cycle numbers. On the other hand, the samples show similar columbic efficiencies irrespective of the firing temperature or time as seen in Figure 13c,d.

Figure 14 also shows the rate capabilities of the various samples. The rate capability is generally known to increase with

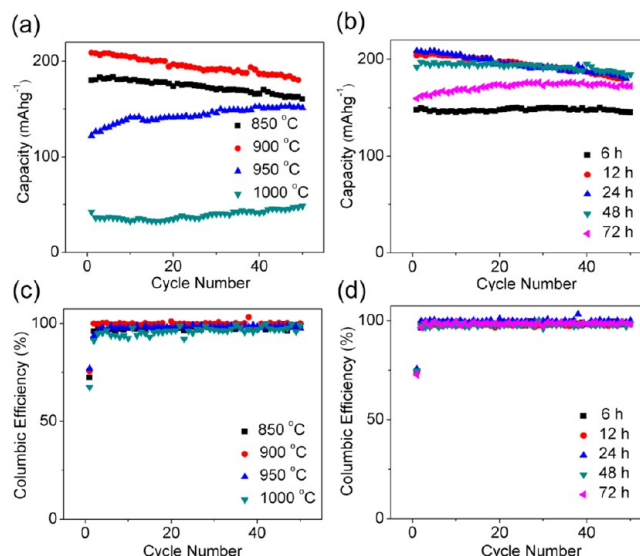


Figure 13. Cyclabilities of $\text{Li}_{1.2}\text{Mn}_{0.6}\text{Ni}_{0.2}\text{O}_2$ fired (a) at various temperatures for 24 h and (b) at 900 °C for various times at 25 mA g^{-1} and columbic efficiencies of $\text{Li}_{1.2}\text{Mn}_{0.6}\text{Ni}_{0.2}\text{O}_2$ fired (c) at various temperatures for 24 h and (d) at 900 °C for various times.

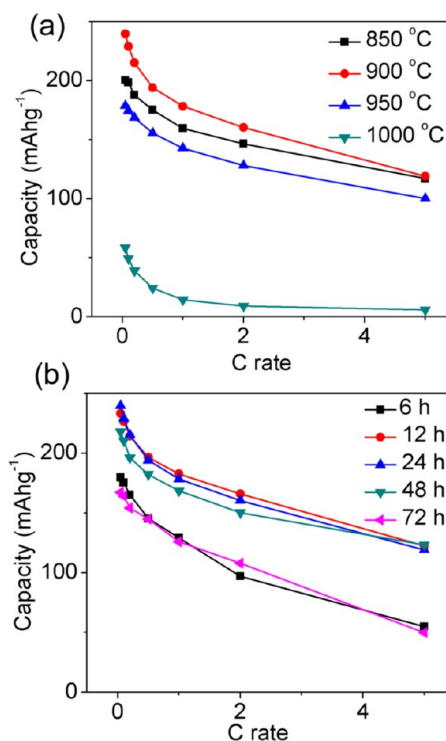


Figure 14. Rate capability of $\text{Li}_{1.2}\text{Mn}_{0.6}\text{Ni}_{0.2}\text{O}_2$ fired (a) at various temperatures for 24 h and (b) at 900 °C for various times.

decreasing particle size,^{36–38} but the particle size effect on the rate capability is not that pronounced in the present case compared to other factors, as discussed below. The samples fired at 850 and 950 °C for 24 h and those fired at 900 °C for 12, 24, and 48 h show similar rate capabilities. In contrast, the samples fired at 1000 °C for 24 h and at 900 °C for 72 h show relatively low rate capability even though the particle size is only ~ 500 nm larger for the sample fired at 1000 °C for 24 h and 300 nm larger for the sample fired at 900 °C for 72 h compared to that fired at 900 °C for 24 h. This can be related

to the cation intermixing between the lithium and transition metal layers caused by the volatilization of lithium during synthesis at high temperatures. In addition, the sample fired at 900 °C for 6 h also shows a low rate capability despite a smaller particle size of ~300 nm due to the incomplete formation of the layered oxide and cation intermixing between the two layers as indicated by the XRD.

CONCLUSIONS

The effect of synthesis temperature and time on the electrochemical properties of the lithium-rich layered $\text{Li}_{1.2}\text{Mn}_{0.6}\text{Ni}_{0.2}\text{O}_2$ cathode has been investigated systematically. The length (capacity) of the plateau region and consequently the reversible capacity in subsequent cycles are maximized with a sample fired at 900 °C for 24 h. Firing at much higher temperatures (1000 °C) or for prolonged times at 900 °C results in a volatilization of lithium, increase in particle size, and decrease in the length of the plateau region and reversible capacity. While a single C2/m phase with high homogeneity and a lithium content of around 1.16 is formed at firing temperatures of around 900 °C for 24 h, a two-phase mixture consisting of C2/m and $\text{R}\bar{3}\text{m}$ phases with a much lower lithium content of 1.09 is formed on firing at 1000 °C for 24 h. The data reveal that a lithium content of >1.15 is critical to obtain a single C2/m phase and maximize length of the plateau region and discharge capacity. Lithium contents <1.15 results in segregation into two phases, smaller length of the plateau region, and lower discharge capacity. This study demonstrates the importance of lithium content and phase relationships, which are influenced sensitively by the synthesis conditions, in optimizing the electrochemical properties of the high-capacity lithium-rich layered oxide cathodes.

ASSOCIATED CONTENT

Supporting Information

Additional material as discussed in the text. This material is available free of charge via the Internet at <http://pubs.acs.org>.

AUTHOR INFORMATION

Corresponding Author

*E-mail: rmanth@mail.utexas.edu. Tel: (512) 471-1791. Fax: (512) 471-7681.

Notes

The authors declare no competing financial interest.

ACKNOWLEDGMENTS

This work was supported as part of the program "Understanding Charge Separation and Transfer at Interfaces in Energy Materials (EFRC: CST)", an Energy Frontier Research Center funded by the U.S. Department of Energy Office of Science, Office of Basic Energy Sciences, under Award DE-SC0001091. We would like to acknowledge the use of the aberration-corrected STEM at the University of Texas at San Antonio, a facility supported by a grant from the National Institute on Minority Health and Health Disparities (G12MD007591) from the National Institutes of Health. We thank Yu-Sheng Su for his assistance with the surface area measurements.

REFERENCES

- (1) Chebaim, R. V.; Prado, F.; Manthiram, A. *Chem. Mater.* **2001**, *13*, 2951–2957.
- (2) Venkatraman, S.; Shin, Y.; Manthiram, A. *Electrochem. Solid-State Lett.* **2003**, *6*, A9–A12.
- (3) Lu, Z.; MacNeil, D. D.; Dahn, J. R. *Electrochem. Solid-State Lett.* **2001**, *4*, A191–A194.
- (4) Lu, Z.; Beaulieu, L. Y.; Donabarger, R. A.; Thomas, C. L.; Dahn, J. R. *J. Electrochem. Soc.* **2002**, *149*, A778–A791.
- (5) Kang, S. H.; Sun, Y. K.; Amine, K. *Electrochem. Solid-State Lett.* **2003**, *6*, A183–A186.
- (6) Lu, Z.; Chen, Z.; Dahn, J. R. *Chem. Mater.* **2003**, *15*, 3214–3220.
- (7) Park, Y. J.; Hong, Y. S.; Wu, X.; Kwang, S. R.; Chang, S. H. *J. Power Sources* **2004**, *129*, 288–295.
- (8) Thackeray, M. M.; Kang, S. -H.; Johnson, C. S.; Vaughey, J. T.; Hackney, S. A. *Electrochem. Commun.* **2006**, *8*, 1531–1538.
- (9) Fell, C. R.; Carroll, K. J.; Chi, M.; Meng, Y. S. *J. Electrochem. Soc.* **2010**, *157*, A1202–A1211.
- (10) Kang, S. H.; Amine, K. *J. Power Sources* **2003**, *124*, 533–537.
- (11) Chebiam, R. V.; Kannan, A. M.; Prado, F.; Manthiram, A. *Electrochem. Commun.* **2001**, *3*, 624–627.
- (12) Wang, G. X.; Horvat, J.; Bradhurst, D. H.; Liu, H. K.; Dou, S. X. *J. Power Sources* **2000**, *85*, 279–283.
- (13) Armstrong, A. R.; Holzapfel, M.; Novak, P.; Johnson, C. S.; Kang, S.; Thackeray, M. M.; Bruce, P. G. *J. Am. Chem. Soc.* **2006**, *128*, 8694–8698.
- (14) Wu, Y.; Manthiram, A. *Electrochem. Solid-State Lett.* **2006**, *9*, A221–A224.
- (15) Ohzuku, T.; Nagayama, M.; Tsuji, K.; Ariyoshi, K. *J. Mater. Chem.* **2011**, *21*, 10179–10188.
- (16) Deng, Z. Q.; Manthiram, A. *J. Phys. Chem C* **2011**, *115*, 7097–7103.
- (17) Wang, C.-C.; Manthiram, A. *J. Mater. Chem. A* **2010**, *10*, 1039–1043.
- (18) P. Xiao, P.; Deng, Z. Q.; Manthiram, A.; Henkelman, G. *J. Phys. Chem.* **2012**, *116*, 23201–23204.
- (19) Wu, Y.; Manthiram, A. *Electrochem. Solid-State Lett.* **2007**, *10*, A151–A154.
- (20) Ishizuka, A. *Ultramicroscopy* **2001**, *90*, 71–83.
- (21) Reimer, J. N.; Li, W.; Dahn, J. R. *Phys. Rev. B* **1993**, *47*, 8486–8493.
- (22) Rougier, A.; Gravereau, P.; Delmas, C. *J. Electrochem. Soc.* **1995**, *143*, 1168–1175.
- (23) Santhanam, R.; Jones, P.; Sumana, A.; Rambabu, B. *J. Power Sources* **2010**, *195*, 7391–7396.
- (24) Koga, H.; Croguennec, L.; Mannesiez, P.; Ménétrier, M.; Weill, F.; Bourgeois, L.; Duttine, M.; Suard, E.; Delmas, C. *J. Phys. Chem. C* **2012**, *116*, 13497–13506.
- (25) Bréger, J.; Jiang, M.; Dupré, N.; Meng, Y. S.; Shao-Horn, Y.; Ceder, G.; Grey, C. P. *J. Solid State Chem.* **2005**, *178*, 2575–2585.
- (26) Boulineau, A.; Croguennec, L.; Delmas, C.; Weill, F. *Chem. Mater.* **2009**, *21*, 4216–4222.
- (27) Jarvis, K.; Deng, Z.; Allard, L. F.; Manthiram, A.; Ferreira, P. *J. Chem. Mater.* **2011**, *23*, 3614–3621.
- (28) Jarvis, K.; Wang, C.-C.; Manthiram, A.; Ferreira, P. *J. Mater. Chem.* submitted.
- (29) Howie, A. *J. Microsc.* **1979**, *117*, 11–23.
- (30) Lei, C. H.; Bareño, J.; Wen, J. G.; Petrov, I.; Kang, S.-H.; Abraham, D. P. *J. Power Sources* **2008**, *178*, 422–433.
- (31) Bareño, J.; Lei, C. H.; Wen, J. G.; Kang, S.-H.; Petrov, I.; Abraham, D. P. *Adv. Mater.* **2010**, *22*, 1122–1127.
- (32) Jo, M.; Hong, Y. S.; Choo, J.; Cho, J. *J. Electrochem. Soc.* **2009**, *156*, A430–A434.
- (33) Choi, S. H.; Son, J. W.; Yoon, Y. S.; Kim, J. *J. Power Sources* **2006**, *158*, 1419–1424.
- (34) Lee, E. S.; Huq, A.; Chang, H. Y.; Manthiram, A. *Chem. Mater.* **2012**, *24*, 600–612.
- (35) Yu, D. Y. W.; Yanagida, K.; Kato, Y.; Nakamura, H. *J. Electrochem. Soc.* **2009**, *156*, A417–A424.
- (36) Okubo, M.; Hosono, E.; Kim, J.; Enomoto, M.; Kojima, N.; Kudo, T.; Zhou, H.; Honma, I. *J. Am. Chem. Soc.* **2007**, *129*, 7444–7452.

- (37) Sclar, H.; Kovacheva, D.; Zhecheva, E.; Stoyanova, R.; Lavi, R.; Kimmel, G.; Grinblat, J.; Girshevitz, O.; Amalraj, F.; Haik, O.; Zinigrad, E.; Markovsky, B.; Aurbacha, D. J. *J. Electrochem. Soc.* **2009**, *156*, A938–A948.
- (38) Li, D. C.; Muta, T.; Zhang, L. Q.; Yoshio, M.; Noguchi, H. *J. Power Sources* **2004**, *132*, 150–155.